IEEE Open Access Journal of
Power and Energy

Received 13 May 2022; revised 13 October 2022; accepted 23 October 2022. Date of publication 28 October 2022;
date of current version 29 December 2022.

Digital Object Identifier 10.1109/OAJPE.2022.3217793

Unified Grid-Forming/Following Inverter Control

SIJIA GENG[1] (Member, IEEE), AND IAN A. HISKENS[2] (Fellow, IEEE)

[1]Department of Electrical and Computer Engineering, Johns Hopkins University, Baltimore, MD 21218 USA
[2]Department of Electrical Engineering and Computer Science, University of Michigan, Ann Arbor, MI 48109 USA
CORRESPONDING AUTHOR: I. A. HISKENS (hiskens@umich.edu)

ABSTRACT The paper describes an inverter control scheme which incorporates both a phase-locked loop (PLL) for voltage synchronization and power-frequency droop for load sharing. As such, it is a hybrid grid-forming/following controller and offers beneficial characteristics of both. The model describing the dynamic behaviour of the inverter control scheme is presented and connections with grid-forming and grid-following control strategies are considered. A process for black-starting the PLL-based inverter control scheme is described. Case studies explore controller small- and large-disturbance performance under a variety of system conditions.

INDEX TERMS Inverter-based resources, grid-forming/following control, dynamic modelling, dynamic performance.

I. INTRODUCTION

POWER systems are undergoing a significant transition to much greater reliance on renewable and other distributed energy resources (DERs) [1]. Solar photovoltaic (PV) panels, wind turbines, batteries and fuel cells, for example, all connect to power systems through power electronic inverters which possess drastically different dynamic characteristics compared with traditional synchronous generation [2]. Careful control and coordination of inverters is necessary to ensure a successful transition to future inverter-based systems [3].

Control strategies for inverter-based resources tend to be categorized as either grid-following or grid-forming [4], [5]. Most of the DERs that are currently being installed on the grid are of the grid-following type. They have been given that name as they synchronize with (follow) the grid voltage waveform using a phase-locked loop (PLL). The PLL output provides a reference for controlling the voltage that is synthesized by the power electronic switches, and hence controlling the active and reactive power that is output by the inverter. If the grid is de-energized then grid-following inverters cannot operate as they have no voltage for synchronization. Furthermore, if the grid is weak, i.e., the Thévenin (source) impedance is high, then the grid voltage waveform will be susceptible to disturbances from the varying output of the inverter and/or other nearby inverter-based resources. This can lead to poorly damped oscillations or even instability. Such behaviour has been observed in the Australian state of South Australia, for example, where all the synchronous generation has been decommissioned in favour of renewable generation and interconnection with the neighbouring states [6]. To achieve reliable operation it has been necessary for the transmission utility to install four synchronous condensers [7]. Such challenges will become increasingly prevalent as synchronous generation is replaced by ever more grid-following resources.

Grid-forming inverters [8], on the other hand, do not rely on direct synchronization to the grid voltage waveform, as is the case with PLLs, but rather rely on a droop relationship between the active power output and the frequency of the synthesized voltage waveform. This enables them to achieve black-start (establish the voltage on a de-energized network) and to support the voltage of an otherwise weak network. However, questions remain regarding dynamic interactions between grid-following and grid-forming control strategies [9], [10].

This paper presents a novel inverter control scheme that incorporates both PLL and droop control. As such, it does not fit the usual classification of grid-forming and grid-following control schemes [5], [11], [12]. The distinguishing feature of the controller is that it regulates active power by adjusting the phase angle across the filter inductance. It has some mathematical similarity to virtual synchronous machine implementations [13], though the motivation and dynamic performance are quite different. As will be shown in later developments, the proposed control scheme inherits characteristics of both grid-forming and grid-following inverter controls. This hybrid control strategy has

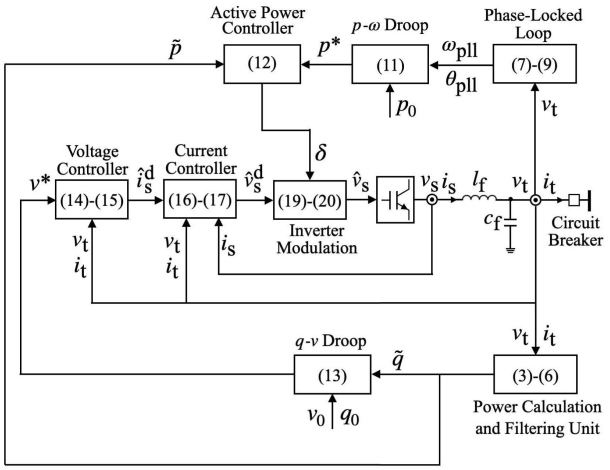

FIGURE 1. Schematic representation of the inverter control scheme.

evolved from earlier work [14], [15] which focused on autonomous switching of microgrids from grid connected to islanded, and vice versa. That earlier control design has been extended to incorporate lower-level cascaded voltage and current control, and addresses the fast dynamics of the output filter and the transmission network.

The following contributions are made throughout the paper:

- A novel control strategy that offers hybrid grid-forming and grid-following characteristics.
- A black-start process for PLL-based controls.
- A straightforward mechanism for low voltage ride through during faults.
- A power flow formulation that takes into account the frequency dependence of impedances/admittances.
- A variety of case studies using benchmark power systems.

The paper is organized as follows. The inverter control scheme is presented in Section II. An overview of system modelling is provided in Section III and case studies are explored in Section IV. Conclusions and future directions are provided in Section V.

II. INVERTER MODEL AND CONTROL

The inverter control scheme is presented schematically in Fig. 1. The controller regulates the voltage magnitude $|v_t|$ at the grid connection point and the active power p delivered to the grid. The control scheme consists of a power calculation and filtering block, a phase-locked loop (PLL), p-ω droop and q-v droop, an active power controller and cascaded voltage and current controllers.

A. REFERENCE FRAMES

1) GLOBAL REFERENCE FRAME

We adopt the common practice of establishing a global rotating DQ-frame as a reference for transforming sinusoidal quantities into (nearly) constant quantities. The rotational velocity (frequency) of this reference frame is given by $\omega_{DQ}\omega_b$ rad/s, where ω_{DQ} is the per unit frequency of the DQ-frame and ω_b is the per unit base for frequency, e.g., $2\pi 60$ rad/s in North America.

It is common for ω_{DQ} to be chosen as the nominal frequency $\omega_{DQ} = \omega_0 = 1$ pu. However, such a choice is arbitrary, and may not be the most useful [16]. In particular, power systems generally operate at a steady-state frequency which is not quite equal to the nominal frequency ω_0. For example, a 60 Hz system may operate at (say) 59.95 Hz. If the steady-state frequency is ω_{ss} (in per unit) and the DQ-frame is rotating at ω_0, then quantities viewed from the DQ-frame will appear to be oscillating at a frequency of $(\omega_{ss} - \omega_{DQ})$ pu. In other words, they are not constant, and therefore are not truly in steady state.

This anomaly can be corrected by solving for equilibrium using a power flow that takes into account the frequency dependence of droop characteristics and impedances/admittances.[1] The resulting power flow solution will provide the steady-state frequency ω_{ss} which can then be used for the DQ-frame, $\omega_{DQ} = \omega_{ss}$. Only then will quantities viewed from the DQ-frame appear constant at steady state.

Voltages and currents across the network are expressed in the global DQ-frame. For each bus this gives,

$$v_t = v_t^D + jv_t^Q = |v_t|\angle\theta_t \tag{1}$$

$$i_t = i_t^D + ji_t^Q. \tag{2}$$

2) LOCAL REFERENCE FRAMES

Control of each individual inverter i uses a local dq-frame rotating at frequency $(\omega_i + \omega_0)$ pu, where the per unit frequency deviation ω_i is determined by the inverter's PLL. These local rotating reference frames are illustrated in Fig. 2. The terminal voltage and current of each inverter can be expressed in the local dq-frame as $v_t^d + jv_t^q$ and $i_t^d + ji_t^q$, respectively. Fig. 3 shows the terminal voltage of an inverter in both the DQ- and dq-frames.

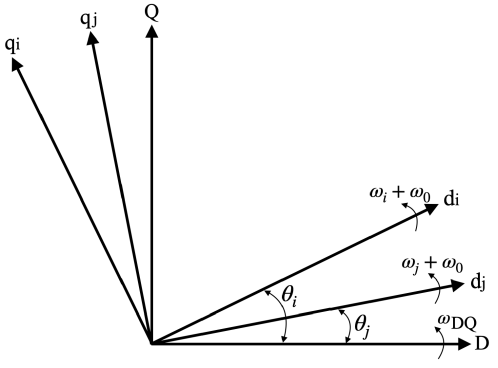

FIGURE 2. Local (dq) and global (DQ) rotating reference frames.

[1]Frequency dependence of network elements is considered further in Section II-I.2.

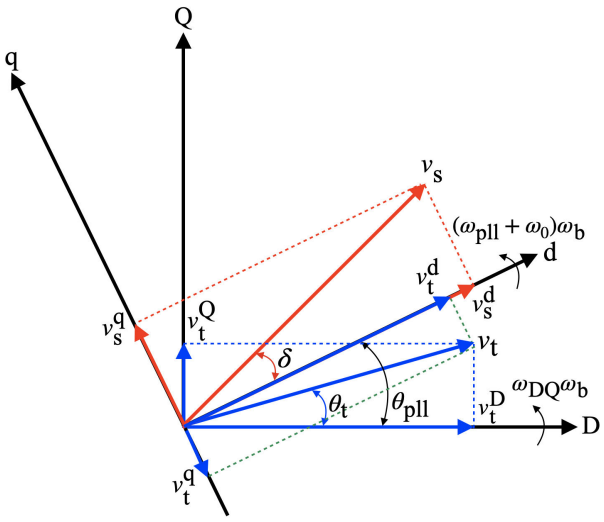

FIGURE 3. **Vector arrangement for the inverter model.**

In order to establish a consistent system-wide representation of the power system, the local dq-frame variables must be transformed to the global DQ-frame. This transformation is provided in Section II-J.

B. POWER CALCULATION AND FILTERING

Active and reactive power of each inverter are computed using dq-frame voltage and current. The computed values are filtered through a low-pass filter to remove high frequency components of the electrical quantities. The equations are given by,

$$p = v_t^d i_t^d + v_t^q i_t^q \tag{3}$$
$$q = v_t^q i_t^d - v_t^d i_t^q \tag{4}$$
$$\dot{\tilde{p}} = \omega_c(p - \tilde{p}) \tag{5}$$
$$\dot{\tilde{q}} = \omega_c(q - \tilde{q}) \tag{6}$$

where p and q are the instantaneous active and reactive power measured at the inverter terminal bus, i.e., the grid connection point, and $\tilde{p}$ and $\tilde{q}$ are the filtered versions of the active and reactive power. The parameter ω_c is the cut-off frequency of each low-pass filter.

C. PHASE-LOCKED LOOP

1) PLL CONTROL

The inverter control scheme makes use of an internal AC waveform that replicates, as closely as possible, the terminal bus voltage. This is typically achieved using a PLL. The PLL adjusts the phase of its internal AC signal so that it synchronizes with the terminal bus voltage, i.e., the PLL signal and the terminal bus voltage are in-phase. This is achieved by driving the angle difference $(\theta_t - \theta_{pll})$ to zero, where θ_t is defined in (1) as the phase of the terminal voltage relative to the DQ-frame and θ_{pll} is the phase of the PLL internal signal relative to that same frame.[2] The PLL angle θ_{pll} serves as an estimate of the terminal voltage angle θ_t and provides a reference for the inverter controller. It is therefore convenient to align the local dq-frame with θ_{pll} as shown in Fig. 3. Also, the PLL frequency $(\omega_{pll} + \omega_0)$, in per unit, provides a filtered version of the terminal bus frequency, and is also available for inverter control.

The PLL dynamics can be written in the form,

$$\dot{\xi} = \theta_t - \theta_{pll} \tag{7}$$
$$\omega_{pll} = K_{pll,p}(\theta_t - \theta_{pll}) + K_{pll,i}\xi \tag{8}$$
$$\dot{\theta}_{pll} = (\omega_{pll} + \omega_0 - \omega_{DQ})\omega_b, \tag{9}$$

where ξ is the integrator state, θ_t is obtained from (1) as,

$$0 = v_t^D \sin\theta_t - v_t^Q \cos\theta_t, \tag{10}$$

and the parameters $K_{pll,p}$ and $K_{pll,i}$ are the proportional and integral gains, respectively. Referring to Fig. 3, $\dot{\theta}_{pll}$ is determined by the difference in the rotational velocities of the dq-frame $(\omega_{pll} + \omega_0)\omega_b$ and the DQ-frame $\omega_{DQ}\omega_b$.

It can be seen from Fig. 3 that driving $\theta_t - \theta_{pll}$ to zero is equivalent to aligning the d-axis of the local dq-frame with the terminal voltage. Therefore, at steady state, $v_t^d = |v_t|$ and $v_t^q = 0$.

Fast PLL dynamic response implies fast phase locking. However, fast response also makes the PLL susceptible to noise. Therefore, a careful trade-off is required to achieve a balance between fast response and noise suppression.

2) PLL-BASED GRID-FORMING INVERTERS

Grid-forming inverters are required to offer black-start capability, which is seemingly in conflict with the use of a PLL. However, assuming the inverter is connected to the grid via a circuit breaker (CB) as shown in Fig. 1, then black-start can be achieved through the following start-up sequence:

1) With the circuit breaker open, energize the power electronic inverter at a fixed frequency determined by an internal oscillator. This will energize the LC filter (which is disconnected from the grid).
2) Synchronize the PLL to the filter voltage v_t and switch inverter voltage control from the fixed-frequency oscillator to the PLL.
3) Close the circuit breaker to energize the network. (As with black-start of any source, the load on the network must be compatible with the capability of the inverter-based source.)

If the inverter is connecting to an already energized network, rather than black-start, then step 3 should make use of a synchronism-check relay (device number 25 in [17]) to ensure the voltages on both sides of the circuit breaker are close to equal. The inverter voltage waveform can be adjusted by internal control to achieve synchronism.

[2]It is important to note that θ_t and θ_{pll} are indeterminable in an absolute sense as no physical reference exists. However, the phase difference $(\theta_t - \theta_{pll})$ is measurable.

This procedure was used in the physical implementation of this control scheme described in [15].

D. ACTIVE POWER CONTROL AND p-ω DROOP

The p-ω droop characteristic is implemented in the form,

$$p^* = p^0 - m_p \omega_{\text{pll}}, \tag{11}$$

where p^0 is the active power set-point at nominal frequency ω_0, ω_{pll} is the per unit deviation of the PLL frequency from ω_0, the parameter m_p is the inverse of the p-ω droop constant, and p^* is the resulting active power set-point. Load sharing between inverters can be achieved by appropriate choice of the inverter droop parameters, just as for traditional synchronous machines. An overload mitigation controller [18] is implemented to ensure that the inverter is never over- or under-loaded.

An integral controller is used to drive the filtered active power $\tilde{p}$ to its set-point p^*. This is achieved through,

$$\dot{\delta} = K_{\text{p,i}}(p^* - \tilde{p}), \tag{12}$$

where δ is the phase angle difference between the inverter source voltage v_{s} and the d-axis of the local dq-frame, as shown in Fig. 3, and $K_{\text{p,i}}$ is the integral gain.

The efficacy of this control scheme lies in the fact that δ is (approximately) the angle of the voltage across the filter inductance l_{f}. The active power produced by the inverter is $p \approx \frac{|v_{\text{s}}||v_{\text{t}}|}{\omega_0 l_{\text{f}}} \sin\delta$, so regulating δ provides direct control of the active power. Most grid-forming active power control strategies effectively regulate the angle across the network's Thévenin impedance [19], which may vary substantially with system operation. It is therefore difficult to tune the controller for wide-ranging conditions, and can, in fact, lead to destabilizing interactions between nearby inverters. In contrast, by utilizing the fixed (internal) impedance $\omega_0 l_{\text{f}}$, the control scheme becomes largely independent of the (external) network conditions.

E. LOW VOLTAGE RIDE THROUGH

The inverter control scheme does not yet precisely implement low voltage ride through (LVRT) requirements such as those prescribed by IEEE standards [20] and various grid codes [21]. However, the structure of the active power controller (12) motivates a straightforward strategy for achieving LVRT. Low voltages on the grid tend to result in a large mismatch $(p^* - \tilde{p})$, with the integral controller potentially causing δ to undergo a large deviation. Two strategies have been employed to prevent such an outcome. Firstly, the terminal voltage v_{t} and current i_{t} are monitored and the apparent impedance $v_{\text{t}}/i_{\text{t}}$ is computed. As with distance protection [22], if the apparent impedance enters a zone that suggests a nearby fault, the integrator (12) is blocked. It remains blocked until the fault is cleared and the apparent impedance returns to normal. Secondly, non-windup limits [23] are implemented on (12) so that δ cannot undergo unrealistic excursions.

F. GRID-FOLLOWING VERSUS GRID-FORMING

Grid-following inverters are generally associated with the use of a PLL to determine grid frequency whereas grid-forming inverters use p-ω droop to establish the frequency [5], [12]. Numerous higher-level power and voltage controllers have been proposed [11], but fundamentally grid-following and grid-forming inverters differ in their approach to synchronization control, either PLL or droop.

In contrast, it follows from Sections II-C and II-D that the proposed inverter control scheme incorporates both PLL and droop control. This hybrid control strategy inherits desirable characteristics of both grid-forming and grid-following inverters. For example, it is shown in Section IV that the hybrid controller performs well under both weak network conditions (which are troublesome for grid-following inverters) and strong networks (when grid-forming inverters are prone to instability).

From (11), it can be seen that when $m_p = 0$ (droop is infinite), the inverter frequency is solely determined by the PLL, according to (7)-(9). Therefore, under this condition, the hybrid controller effectively reverts to grid-following.

G. REACTIVE POWER q-v DROOP

A droop characteristic is also implemented to establish dependence of the terminal voltage set-point on the reactive power output,

$$v^* = v^0 - m_q(\tilde{q} - q^0), \tag{13}$$

where v^0 is the nominal terminal voltage set-point when the reactive power output takes the nominal value q^0, m_q is the reactive power droop constant, and v^* is the resulting terminal voltage set-point.

H. VOLTAGE CONTROL

1) INNER-LOOP CASCADED VOLTAGE AND CURRENT CONTROLLERS

Cascaded voltage and current controllers are widely used in inverter control [19], [24]. They are designed to suppress high frequency disturbances and damp the output LC filter. However, in contrast with standard cascaded voltage and current controllers, the following controller only considers the d-axis variables. This reflects the novel structure of the control scheme, which exploits angle difference δ for active power control and manipulates v_{s}^{d} for voltage control.

The voltage controller is described by,

$$\dot{\phi}_{\text{d}} = v^* - v_{\text{t}}^{\text{d}} \tag{14}$$

$$\hat{i}_{\text{s}}^{\text{d}} = k_{\text{p}}^v(v^* - v_{\text{t}}^{\text{d}}) + k_{\text{i}}^v\phi_{\text{d}} + k_{\text{f}}^v i_{\text{t}}^{\text{d}} - (\omega_{\text{pll}} + \omega_0)c_{\text{f}}v_{\text{t}}^{\text{q}} \tag{15}$$

where $\hat{i}_{\text{s}}^{\text{d}}$ is the desired value for i_{s}^{d}, ϕ_{d} is the integrator state, and k_{p}^v, k_{i}^v, k_{f}^v are the proportional, integral and feedforward gains, respectively. The parameter c_{f} denotes filter capacitance in per unit.

The current controller is described by,

$$\dot{\gamma}_{\text{d}} = \hat{i}_{\text{s}}^{\text{d}} - i_{\text{s}}^{\text{d}} \tag{16}$$

$$\hat{v}_{\text{s}}^{\text{d}} = k_{\text{p}}^i(\hat{i}_{\text{s}}^{\text{d}} - i_{\text{s}}^{\text{d}}) + k_{\text{i}}^i\gamma_{\text{d}} + k_{\text{f}}^i v_{\text{t}}^{\text{d}} - (\omega_{\text{pll}} + \omega_0)l_{\text{f}}i_{\text{s}}^{\text{q}} \tag{17}$$

where $\hat{v}_s^d$ is the desired value for v_s^d, γ_d is the integrator state, and k_p^i, k_i^i, k_f^i are the proportional, integral and feedforward gains, respectively. The parameter l_f denotes the filter inductance in per unit.

2) SINGLE-LOOP VOLTAGE CONTROL

A simpler voltage control scheme exploits the direct relationship between the inverter source voltage magnitude $|v_s|$ and the terminal voltage magnitude $|v_t|$,

$$|\dot{\hat{v}}_s| = K_{v,i}(v^* - |v_t|), \tag{18}$$

where $K_{v,i}$ is the integral gain. It is shown in [19] that the performance of this voltage control scheme is at least as good as that of the cascaded controller.

3) INVERTER MODULATION

The cascaded controller provides the set-point $\hat{v}_s^d$ for the d-axis component of the inverter source voltage, whereas the single-loop controller of Section II-H.2 provides the set-point magnitude $|\hat{v}_s|$. In both cases, the active power controller provides the set-point for the inverter source voltage angle δ (relative to the d-axis). These set-points are supplied to a PWM block to provide a modulation signal for the inverter. For simplicity, we assume that the inverter source voltage can be perfectly regulated to the set-point, so $v_s^d = \hat{v}_s^d$ or alternatively $|v_s| = |\hat{v}_s|$. The unknowns can be obtained from,

$$|v_s|\cos\delta = v_s^d \tag{19}$$
$$|v_s|\sin\delta = v_s^q, \tag{20}$$

where v_s^q is the q-axis component of v_s.

I. CIRCUIT ELEMENTS

1) OUTPUT LC FILTER

An output LC filter is standard for eliminating undesired switching frequency components from the output current spectrum [25]. The inductor is designed to limit current ripple, while the capacitor and inductor are tuned to filter high frequency harmonics.

Based on the circuit equations derived in Appendix A, the dynamics of the output LC filter are given by,

$$\dot{i}_s^d = \frac{\omega_b}{l_f}(v_s^d - v_t^d) + (\omega_{pll} + \omega_0)\omega_b i_s^q \tag{21}$$
$$\dot{i}_s^q = \frac{\omega_b}{l_f}(v_s^q - v_t^q) - (\omega_{pll} + \omega_0)\omega_b i_s^d \tag{22}$$
$$\dot{v}_t^d = \frac{\omega_b}{c_f}(i_s^d - i_t^d) + (\omega_{pll} + \omega_0)\omega_b v_t^q \tag{23}$$
$$\dot{v}_t^q = \frac{\omega_b}{c_f}(i_s^q - i_t^q) - (\omega_{pll} + \omega_0)\omega_b v_t^d, \tag{24}$$

where i_s^{dq} is the current flowing through the inductor and i_t^{dq} is the current flowing to the grid, as shown in Fig. 1. Also, v_s^{dq} and v_t^{dq} are the source and terminal voltage of the inverter, respectively. All variables are in per unit, as are the filter inductance l_f and capacitance c_f.

2) DYNAMIC LINE MODEL

Phasors are typically adopted for line models when analyzing power systems that are dominated by synchronous generation. Fast line dynamics are omitted and frequency is assumed to take the nominal value ω_0. However, as inverter-based resources grow, it is becoming increasingly important to include the fast line dynamics to capture potential dynamic interactions of inverters with and through the network.

Consider a transmission line or feeder connecting buses i and j with series resistance r_{ij} and inductance l_{ij}, both in per unit. It follows from Appendix A that the dynamic line model is given by,

$$\dot{i}_{ij}^D = \frac{\omega_b}{l_{ij}}(v_i^D - v_j^D) - \left(\frac{r_{ij}}{l_{ij}}\omega_b i_{ij}^D - \omega_{DQ}\omega_b i_{ij}^Q\right) \tag{25}$$
$$\dot{i}_{ij}^Q = \frac{\omega_b}{l_{ij}}(v_i^Q - v_j^Q) - \left(\frac{r_{ij}}{l_{ij}}\omega_b i_{ij}^Q + \omega_{DQ}\omega_b i_{ij}^D\right) \tag{26}$$

where i_{ij}^{DQ} is the current flowing through the line branch from bus i to bus j. Similarly, the equations governing line shunt capacitance follow directly from Appendix A.

3) STEADY STATE

At steady state, the dynamic model of the output filter (21)-(24) reverts to a set of algebraic equations that can be expressed as,

$$v_s^d - v_t^d = -(\omega_{pll} + \omega_0)l_f i_s^q \tag{27}$$
$$v_s^q - v_t^q = (\omega_{pll} + \omega_0)l_f i_s^d \tag{28}$$
$$i_s^d = i_t^d - (\omega_{pll} + \omega_0)c_f v_t^q \tag{29}$$
$$i_s^q = i_t^q + (\omega_{pll} + \omega_0)c_f v_t^d. \tag{30}$$

These equations can be written compactly in complex form,

$$(v_s^d + jv_s^q) - (v_t^d + jv_t^q) = j(\omega_{pll} + \omega_0)l_f(i_s^d + ji_s^q) \tag{31}$$
$$(i_s^d + ji_s^q) - (i_t^d + ji_t^q) = j(\omega_{pll} + \omega_0)c_f(v_t^d + jv_t^q). \tag{32}$$

Note that this is the phasor representation of the filter, though with per unit frequency $\omega_{pll} + \omega_0$.

In determining the steady-state representation of the line model (25)-(26), two cases will be considered. In the first case, assume $\omega_{DQ} = \omega_{ss}$, the steady-state frequency. Then at steady-state, electrical quantities viewed from the DQ-frame are constant, so the derivatives in (25)-(26) are zero. This results in the algebraic line model,

$$v_i^D - v_j^D = r_{ij}i_{ij}^D - \omega_{ss}l_{ij}i_{ij}^Q \tag{33}$$
$$v_i^Q - v_j^Q = r_{ij}i_{ij}^Q + \omega_{ss}l_{ij}i_{ij}^D. \tag{34}$$

In the second, more general case, the system at steady-state may operate at a frequency $\omega_{ss} \neq \omega_{DQ}$. Then at steady-state, the electrical quantities represented in the DQ-frame are sinusoidal with frequency $\omega_{ss} - \omega_{DQ}$. It follows from the definition of DQ-frame quantities that $\dot{i}_{ij}^D = -(\omega_{ss} - \omega_{DQ})\omega_b i_{ij}^Q$ and $\dot{i}_{ij}^Q = (\omega_{ss} - \omega_{DQ})\omega_b i_{ij}^D$. Substituting into (25)

and (26) gives,

$$-(\omega_{ss}-\omega_{DQ})\omega_b i_{ij}^{Q}=\frac{\omega_b}{l_{ij}}(v_i^{D}-v_j^{D})-\Big(\frac{r_{ij}}{l_{ij}}\omega_b i_{ij}^{D}-\omega_{DQ}\omega_b i_{ij}^{Q}\Big)$$
$$(\omega_{ss}-\omega_{DQ})\omega_b i_{ij}^{D}=\frac{\omega_b}{l_{ij}}(v_i^{Q}-v_j^{Q})-\Big(\frac{r_{ij}}{l_{ij}}\omega_b i_{ij}^{Q}+\omega_{DQ}\omega_b i_{ij}^{D}\Big).$$

Cancelling like terms and rearranging gives exactly (33)-(34), which can be rewritten in complex form,

$$(v_i^{D}+jv_i^{Q})-(v_j^{D}+jv_j^{Q})=(r_{ij}+j\omega_{ss}l_{ij})(i_{ij}^{D}+ji_{ij}^{Q}). \tag{35}$$

This is the phasor representation of the line, though with per unit frequency ω_{ss} rather than the more common frequency ω_0 that is generally used to define phasors [16], [26].

Power flow modifications that take into account such frequency-dependent impedances are outlined in Appendix B. Whilst it is clear that the dependence of impedances on ω_{ss} will result in very little alteration to power flow solutions, it is often important to determine exact equilibrium conditions.

J. TRANSFORMING LOCAL DQ-FRAME VARIABLES TO THE GLOBAL DQ-FRAME

Define the rotation matrix $\mathcal{R}(\theta)$ parameterized by the angle θ,

$$\mathcal{R}(\theta)=\begin{bmatrix}\cos\theta & -\sin\theta\\ \sin\theta & \cos\theta\end{bmatrix}, \tag{36}$$

where θ denotes the angle of the local dq-frame with respect to the global DQ-frame, as depicted in Fig. 2. It follows that,

$$\mathcal{R}(\theta)^{-1}=\mathcal{R}(-\theta). \tag{37}$$

Since the angle of the inverter local dq-frame is specified by the PLL angle θ_{pll}, the transformation is expressed as,

$$\begin{bmatrix}v_t^{D}\\ v_t^{Q}\end{bmatrix}=\mathcal{R}(\theta_{pll})\begin{bmatrix}v_t^{d}\\ v_t^{q}\end{bmatrix} \tag{38}$$
$$\begin{bmatrix}i_t^{D}\\ i_t^{Q}\end{bmatrix}=\mathcal{R}(\theta_{pll})\begin{bmatrix}i_t^{d}\\ i_t^{q}\end{bmatrix}, \tag{39}$$

where v_t^{DQ} and i_t^{DQ} are the inverter terminal voltage and current with respect to the global DQ-frame.

III. SYSTEM MODELLING AND ANALYSIS

The model of an inverter-based source consists of the eleven differential equations (5)-(7), (9), (12), (14), (16), (21)-(24), together with the fourteen algebraic equations (3)-(4), (8), (10)-(11), (13), (15), (17), (19)-(20), (38)-(39). Each such source connects to the remainder of the power system through its terminal voltage $v_t=v_t^{D}+jv_t^{Q}$ and current $i_t=i_t^{D}+ji_t^{Q}$ (as viewed from the system-wide DQ-frame).

An object-oriented approach for assembling all the components of a power system is presented in [27]. Using that approach, each component is described individually in terms of its differential-algebraic equations (DAEs), allowing all of its partial derivatives to be computed symbolically. Those equations and partial derivatives are then assembled through an automated process to form the system-wide DAE model,

$$\dot{x}=f(x,y) \tag{40}$$
$$0=g(x,y), \tag{41}$$

and its associated Jacobian matrices, which form the linearized DAE model,

$$\begin{bmatrix}\Delta\dot{x}\\ 0\end{bmatrix}=\begin{bmatrix}\frac{\partial f}{\partial x} & \frac{\partial f}{\partial y}\\ \frac{\partial g}{\partial x} & \frac{\partial g}{\partial y}\end{bmatrix}\begin{bmatrix}\Delta x\\ \Delta y\end{bmatrix}. \tag{42}$$

To assess small disturbance stability, as is undertaken in Section IV-A, the algebraic states Δy are eliminated to effectively[3] give,

$$\Delta\dot{x}=\Big(\frac{\partial f}{\partial x}-\frac{\partial f}{\partial y}\Big(\frac{\partial g}{\partial y}\Big)^{-1}\frac{\partial g}{\partial x}\Big)\Delta x=A\Delta x. \tag{43}$$

The eigen-structure of A establishes the (small disturbance) stability properties of the equilibrium point [29].

Consequently, Newton-based algorithms can be used to determine steady-state (extended power flow) conditions. Eigenvalues, eigenvectors and participation factors can be computed directly for small-disturbance analysis. Furthermore, the assembled equations and matrices can be used in implicit numerical integration algorithms to compute trajectories and trajectory sensitivities [27], [30]. This process was used to generate the case studies of Section IV.

A succinct discussion of power system models, in particular inverter, generator and network models, is provided in [16]. The approach adopted there has a more system-theoretic flavour than this paper. Nevertheless, there is consistency in the two modelling formulations.

IV. CASE STUDIES

A. SINGLE INVERTER

The dynamic performance of inverter-based resources depends fundamentally upon the strength of the network to which they are connected. Furthermore, as discussed in Section II-D, the active power droop parameter m_p effectively determines whether a source behaves as grid-following ($m_p=0$) or grid-forming ($m_p>0$). This first case study explores these factors through the use of a simple system composed of an inverter connected to a Thévenin equivalent, as shown in Fig. 4. Parameter values for the inverter are given in Table 1, except for m_p which takes values that depend on the study. In all cases, the inverter is initially operating in steady state supplying active power $p=p^0=0.5$ pu. At 0.2 s, the active power set-point undergoes a step to $p^0=0.7$ pu.

Fig. 5 shows the response of the active power output of the inverter for three values of the Thévenin impedance,[4] $x=0.2$ pu, 0.8 pu, 1.4 pu (with $m_p=100$ in all cases). It is clear that as the system becomes weaker (higher values of x),

[3]Restructuring as a generalized eigenvalue problem [28] allows the eigenvalues of A to be determined without inverting $\frac{\partial g}{\partial y}$.

[4]An impedance-based line model is sufficient for this case study as the fast line dynamics have no influence on behaviour in this example.

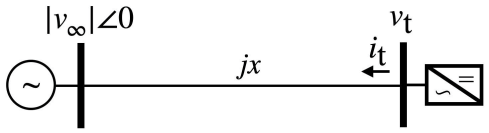

FIGURE 4. **Thévenin equivalent network with inverter-based source.**

TABLE 1. **Parameters of the inverter.**

Parameter	Symbol	Value	Unit
Low-pass filter cutoff frequency	ω_c	50	rad/s
Active power control integral gain	$K_{\text{p,i}}$	0.3	pu
PLL integral gain	$K_{\text{pll,i}}$	5.0	pu
PLL proportional gain	$K_{\text{pll,p}}$	0.2	pu
Reference input for active power	p^0	0.5	pu
Reference input for voltage	v^0	1	pu
Reference input for reactive power	q^0	0.1	pu
Droop gain for active power	m_p	100	-
Droop gain for reactive power	m_q	0.05	-
Base value of frequency	ω_b	$2\pi 60$	rad/s
Voltage control proportional gain	k_p^v	1	-
Voltage control integral gain	k_i^v	2	-
Voltage control feedforward gain	k_f^v	1	-
Current control proportional gain	k_p^i	1	-
Current control integral gain	k_i^i	2	-
Current control feedforward gain	k_f^i	0	-
Output filter capacitance	c_f	0.074	pu
Output filter inductance	l_f	0.08	pu

the step response becomes progressively more over-damped. This can be explained by recalling that $p = \frac{|v_t||v_\infty|}{x}\sin\theta_t$ for the system of Fig. 4. As x increases, the sensitivity $\frac{\Delta p}{\Delta\theta_t}$ reduces. The inverter control scheme regulates active power by varying the phase of the inverter voltage v_s (relative to the rotating DQ-frame reference). Therefore the reduced sensitivity implies that a larger change in phase angle is required to achieve the specified change in active power. It is worth noting that for the system of Fig. 4, maximum power transfer (determined by a saddle-node bifurcation) corresponds to $p_{max} \approx 1/x$. For the case shown in Fig. 5 with $x = 1.4$ pu, maximum power is $p_{max} = 1/1.4 = 0.714$ pu. Hence, the inverter controller exhibits admirable performance by robustly driving the active power output $p = 0.7$ pu so close to that limit.

Fig. 6 shows the influence of the active power droop parameter m_p on the inverter step response. For $m_p = 100$ and 400, the inverter is grid-forming and displays well-damped step response. Damping increases with increasing m_p. When the inverter active power set-point has no dependence on frequency ($m_p = 0$) it becomes grid-following. In this case behaviour is highly oscillatory, which is consistent with reduced robustness of grid-following inverters in weak networks. Eigenvalue analysis revealed that the system undergoes a Hopf bifurcation when the system

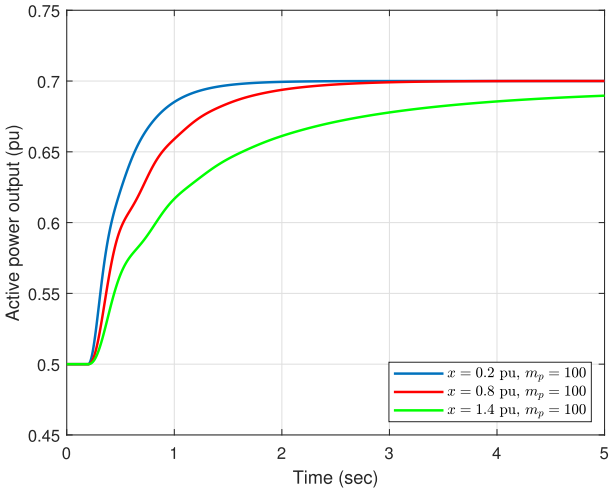

FIGURE 5. **Active power output of the inverter for varying network strength.**

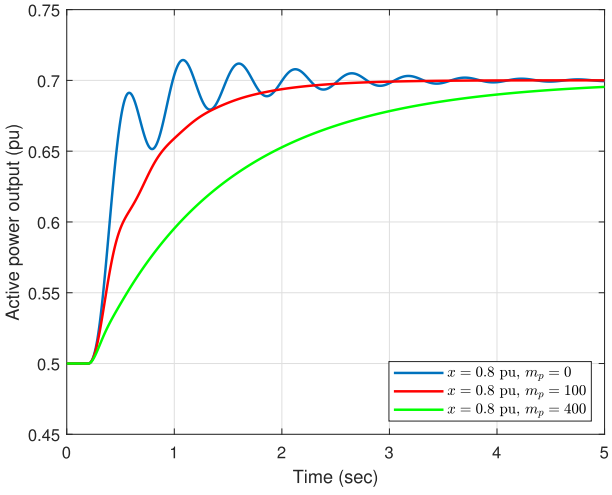

FIGURE 6. **Active power output of the inverter for varying droop parameter m_p.**

impedance is increased slightly to $x = 0.923$ pu. The oscillatory frequency at the bifurcation is 8.67 rad/s (1.38 Hz).

Small disturbance (eigenvalue) analysis can be used to more completely explore the dynamic behaviour of the inverter controller, and in particular to establish the contributions of the various control loops. For this investigation, the line impedance jx between the inverter and the infinite bus was replaced by a dynamic line modelled by (25)-(26). A line inductance value of $l_{12} = 0.8$ pu was chosen to match the impedance $x = 0.8$ pu used in the earlier investigation. A small resistance of $r_{12} = 0.1$ pu was also included. The parameter values given by Table 1 were again used, with equilibrium corresponding to $p^0 = 0.5$ pu.

The DAE model for this system includes thirteen differential equations consisting of the seven controller equations of the inverter-based source, its four filter equations, and the two equations describing the dynamic line (25)-(26). Linearization of the DAE model for this system results

TABLE 2. Eigenvalues for the single inverter network.

Full system $m_p = 100$	Reduced system $m_p = 100$	Reduced system $m_p = 0$
$-2331.8 \pm j6730.6$		
$-65.2 \pm j5107.7$		
$-43.7 \pm j367.6$		
-49.9	-49.9	-49.9
-51.6	-51.5	-51.5
$-5.0 \pm j16.3$	$-5.0 \pm j16.2$	$-1.5 \pm j12.7$
-2.1	-2.1	-3.8
$-1.0 \pm j1.0$	$-1.0 \pm j1.0$	$-1.0 \pm j1.0$

in a 13-dimensional A matrix. The thirteen eigenvalues of A are listed in the left column of Table 2. Notice that the first six eigenvalues have much larger magnitudes than the other seven. The first four of those larger eigenvalues correspond to the filter dynamics, while the other two are associated with the dynamic line. Those six differential equations describe much faster response due to very small time constants. It is therefore possible to apply singular perturbation analysis [31], [32] to replace those differential equations by the algebraic equations obtained when the derivatives are set to zero.[5] The only differential equations remaining in the resulting reduced-order DAE model are the controller equations (5)-(7), (9), (12), (14), (16). The eigenvalues of the corresponding linearized model, which is now 7-dimensional, are given by the centre column of Table 2. Notice that those eigenvalues are almost identical to the lower six eigenvalues obtained for the full model. This indicates that the singular perturbation is a very good approximation.

Participation factors [33] reveal that the first two (real) eigenvalues are associated with the dynamics of the active and reactive power filters (5)-(6). The complex conjugate pair of eigenvalues ($-5.0 \pm j16.2$) displays strong participation of the states ξ, θ_{pll} and δ associated with the PLL and active power control loop. Likewise, the real eigenvalue (-2.1) is dominated by θ_{pll} and δ. These three eigenvalues together indicate a third-order coupling which exhibits relatively slow exponential response that is modulated by well damped oscillations. The final complex conjugate pair of eigenvalues are associated with the dynamics of the voltage and current controllers (14), (16).

When the value of the droop parameter m_p is reduced from 100 to 0, corresponding to grid-following control, the three eigenvalues associated with the PLL and active power control adjust as shown in the right column of Table 2. (Notice that the other eigenvalues are unaffected by the change to m_p.) The larger magnitude of the real eigenvalue indicates more rapid exponential response whereas the complex conjugate pair exhibit lower frequency and reduced damping. These trends are consistent with the results presented in Fig. 6, where a comparison of the two cases clearly shows faster and more oscillatory response when $m_p = 0$. The third-order dynamic interactions between ω_{pll}, θ_{pll} and δ are shown clearly in Fig. 7.

[5]Singular perturbation is possible in this case because the fast dynamics are stable, as indicated by the corresponding eigenvalues all having negative real parts.

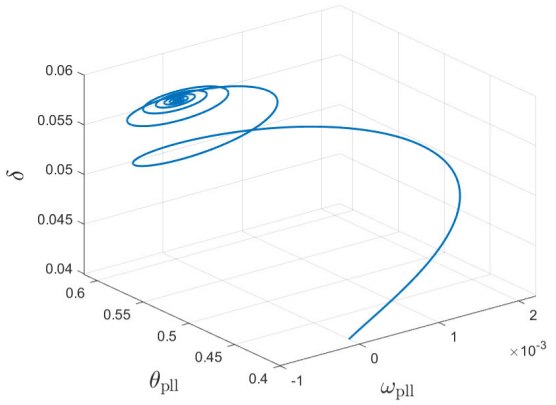

FIGURE 7. Dynamic interaction between ω_{pll}, θ_{pll} and δ for the case in Fig. 6 with $m_p = 0$.

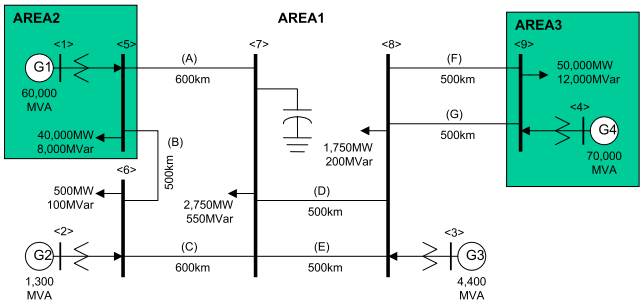

FIGURE 8. Anderson-Farmer test system.

B. ANDERSON-FARMER POWER SYSTEM

The second case study uses the Anderson-Farmer test system which is shown in Fig. 8. It is a three-area, four-generator power system that originates from [34] and was further developed within [35]. Areas 2 and 3 are equivalents of larger power systems, with their generation represented by G1 and G4, respectively. Those two areas are interconnected by Area 1, which incorporates two generators G2 and G3 that are rated at 1300 MVA and 4400 MVA, respectively. Generators G1 and G4 are both represented using the second-order classical machine model. In contrast, generators G2 and G3 are represented by sixth-order synchronous machine models, together with governors, automatic voltage regulators and power system stabilizers. This study replaces those two generators by aggregate inverter-based sources of the form described in Section II. The parameter values given in Table 1 are again used, though with scaling of values where necessary to match the ratings of G2 and G3.

For this study, $m_p = 100$ for G2 and $m_p = 0$ for G3. The study therefore involves a combination of grid-forming and grid-following inverters together with synchronous generators.

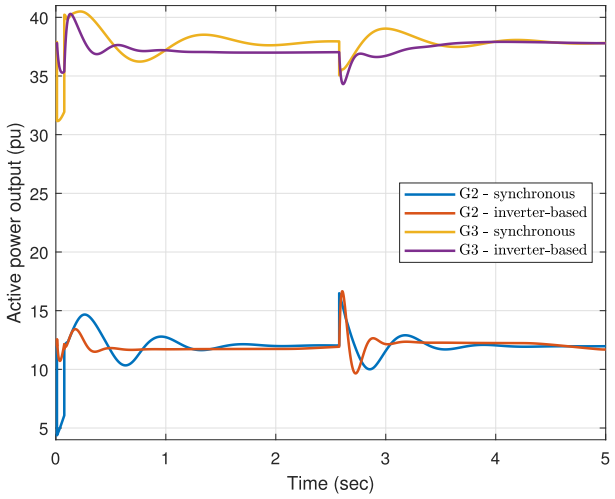

FIGURE 9. **Active power output of generators G2 and G3.**

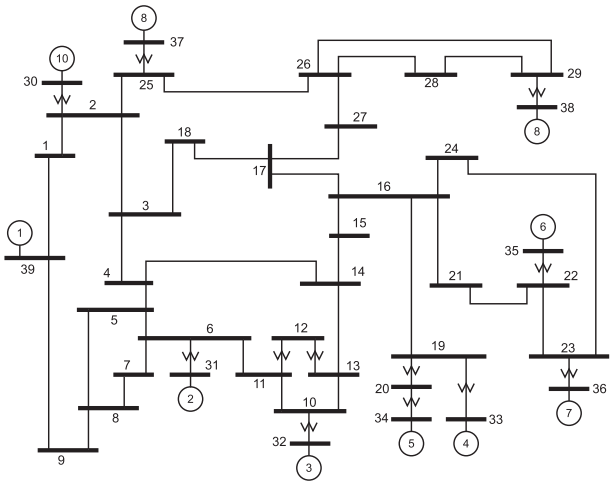

FIGURE 10. **IEEE 39-bus benchmark power system.**

Under normal operation, line 6-7 is heavily loaded at 810 MW, which is a large portion of the 1200 MW output of G2. The outage of this line has a profound impact on Generator G2, in particular, as it causes all of the power production of G2 to be rerouted via lines 5-6 and 5-7, the latter of which is already heavily loaded. This disturbance, therefore, results in quite significant dynamic response of generators G2 and G3.

To study the dynamic behaviour of this system, a solid three-phase fault was applied at the midpoint of line 6-7. The fault was cleared after 0.0667 s (4 cycles) by tripping the line. The line was subsequently reclosed after a further 2.5 s. Fig. 9 shows the active power output of generators G2 and G3, for the original system where they were synchronous machines and for the new situation where they are inverter-based sources.

It can be seen from Fig. 9 that the inverter-based sources exhibit well damped behaviour in response to this significant disturbance. Their active power excursions during the fault-on period are much less than those of the synchronous generators. Likewise, the post-fault oscillations of the inverter-based sources are smaller and better damped than for the synchronous generators. The same is generally true when line 6-7 is reclosed. For G2, the initial post-reclosure response of the inverter-based source is of the same order as the synchronous generator, but the inverter-based source exhibits better damping. Recall that the inverter controls have not been retuned for this example. Rather, the default values from Table 1 have been used. This is testament to the robustness of the control strategy.

C. IEEE 39-BUS POWER SYSTEM

The third case study considers the IEEE 39-bus benchmark power system shown in Fig. 10, with data from [35]. In this case, generators G4 (producing 632 MW) and G7 (producing 560 MW) were replaced by inverter-based sources with matching production. The values of the droop parameters for those two sources were $m_{p,4} = 100$ and $m_{p,7} = 0$, respectively, implying that generator G4 was grid-forming whilst G7 was grid-following. This system was disrupted by a solid three-phase fault on bus 16, which was cleared after 0.1 s. This fault had a significant impact on the four generators G4–G7, inducing interactions between grid-forming, grid-following and synchronous sources.

The base case behaviour, where G4–G7 were all synchronous generators, is shown in Fig. 11. Changing G4 and G7 to inverter-based sources resulted in the response shown in Fig. 12. (The detailed transient response over the initial 0.3 s is provided in Fig. 13.) It can be seen that the grid-forming, grid-following and synchronous sources all work well together, with behaviour being a little better damped than in the base case. The proposed control scheme once again integrates well into established power systems and provides a stabilizing influence.

V. CONCLUSION

The paper introduces a novel inverter control scheme which offers performance advantages over grid-forming and grid-following controls. Improved robustness is achieved by incorporating both power-frequency droop and a phase-locked loop (PLL) into the control strategy. The resulting hybrid controller inherits beneficial characteristics from both droop and the PLL, allowing robust operation over a wide range of system operating conditions. Even though the control scheme involves a PLL, a process is described for achieving black-start energization. The robustness of the hybrid control scheme is explored through a variety of case studies that consider small- and large-disturbance dynamic behaviour.

Future work will seek to establish a clearer understanding of the ways in which inverter-based sources influence modal (inter-machine) oscillations. This will explore the relationship between the network (graph) topology, locations of synchronous and inverter-based sources, and the small-disturbance eigen-structure. We will also further

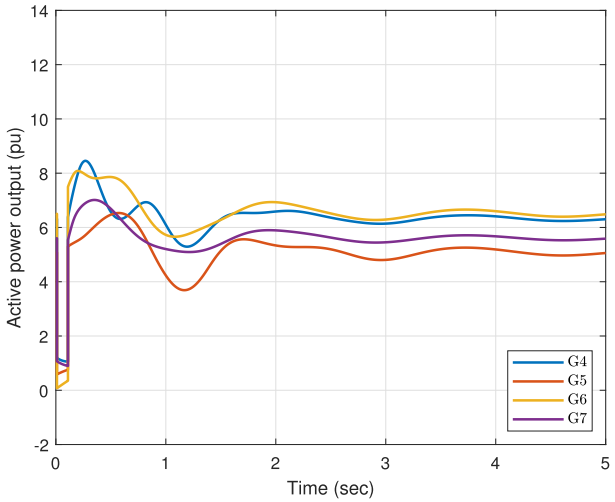

FIGURE 11. Base case active power output, G4–G7 are all synchronous generators.

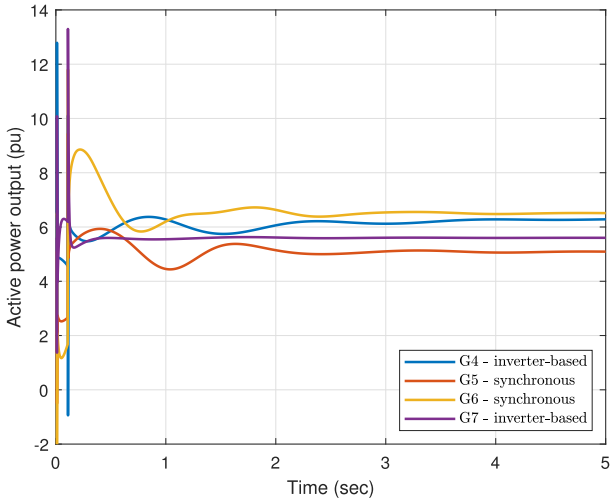

FIGURE 12. Active power output, G4 and G7 are inverter-based sources.

investigate the impact of inverter-based sources on large-disturbance stability, paying particular attention to the role of the third-order coupling between the PLL and active power controls. It is anticipated that Lyapunov theory will provide valuable insights.

APPENDIX A

Consider a balanced three-phase RL branch. Balanced line-to-neutral voltages $\boldsymbol{v}^{\text{abc}} = [v_{\text{a}}\ v_{\text{b}}\ v_{\text{c}}]^{\intercal}$ induce balanced branch currents $\boldsymbol{i}^{\text{abc}} = [i_{\text{a}}\ i_{\text{b}}\ i_{\text{c}}]^{\intercal}$ according to,

$$\boldsymbol{v}^{\text{abc}} = L\frac{d}{dt}\boldsymbol{i}^{\text{abc}} + R\boldsymbol{i}^{\text{abc}}, \tag{44}$$

where R and L are scalars with units of ohms and henries, respectively. Using the power-variant dq0-transformation $\boldsymbol{v}^{\text{dq0}} = T_\theta \boldsymbol{v}^{\text{abc}}$ and $\boldsymbol{i}^{\text{dq0}} = T_\theta \boldsymbol{i}^{\text{abc}}$, where,

$$T_\theta = \frac{2}{3}\begin{bmatrix} \cos\theta & \cos(\theta - \frac{2\pi}{3}) & \cos(\theta + \frac{2\pi}{3}) \\ -\sin\theta & -\sin(\theta - \frac{2\pi}{3}) & -\sin(\theta + \frac{2\pi}{3}) \\ \frac{1}{2} & \frac{1}{2} & \frac{1}{2} \end{bmatrix}, \tag{45}$$

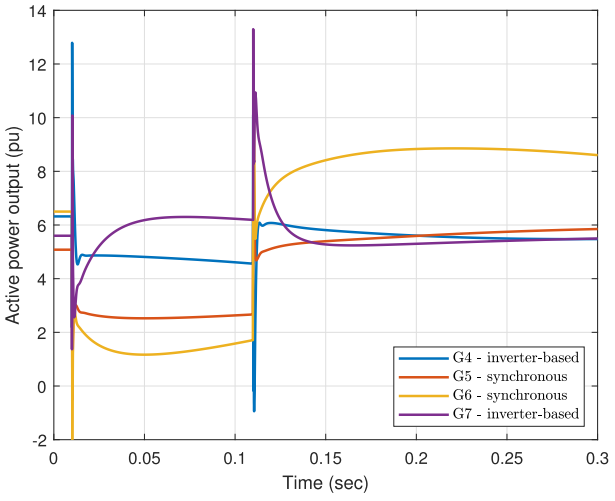

FIGURE 13. Active power output, focusing on the transient period.

the circuit equation (44) can be rewritten,

$$\begin{aligned} T_\theta^{-1}\boldsymbol{v}^{\text{dq0}} &= L\frac{d}{dt}\left(T_\theta^{-1}\boldsymbol{i}^{\text{dq0}}\right) + RT_\theta^{-1}\boldsymbol{i}^{\text{dq0}} \\ &= L\frac{d}{dt}\left(T_\theta^{-1}\right)\boldsymbol{i}^{\text{dq0}} + LT_\theta^{-1}\frac{d}{dt}\left(\boldsymbol{i}^{\text{dq0}}\right) + RT_\theta^{-1}\boldsymbol{i}^{\text{dq0}}. \end{aligned} \tag{46}$$

It is straightforward to show that $\frac{d}{dt}\left(T_\theta^{-1}\right) = -T_\theta^{-1}W$ where,

$$W = \begin{bmatrix} 0 & \frac{d}{dt}\theta & 0 \\ -\frac{d}{dt}\theta & 0 & 0 \\ 0 & 0 & 0 \end{bmatrix}. \tag{47}$$

Therefore (46) can be rewritten,

$$\boldsymbol{v}^{\text{dq0}} = -LW\boldsymbol{i}^{\text{dq0}} + L\frac{d}{dt}\left(\boldsymbol{i}^{\text{dq0}}\right) + R\boldsymbol{i}^{\text{dq0}}. \tag{48}$$

Rearranging gives,

$$\frac{d}{dt}\left(\boldsymbol{i}^{\text{dq0}}\right) = \frac{1}{L}\boldsymbol{v}^{\text{dq0}} + W\boldsymbol{i}^{\text{dq0}} - \frac{R}{L}\boldsymbol{i}^{\text{dq0}}. \tag{49}$$

Transforming to per unit requires the line-to-neutral voltage base V_{b}, line current base I_{b}, impedance base $Z_{\text{b}} = V_{\text{b}}/I_{\text{b}}$, frequency base ω_{b} and inductance base $L_{\text{b}} = Z_{\text{b}}/\omega_{\text{b}}$. Then (49) can be rewritten,

$$\frac{d}{dt}\left(\boldsymbol{i}_{\text{pu}}^{\text{dq0}} I_{\text{b}}\right) = \frac{1}{l_{\text{pu}}L_{\text{b}}}\boldsymbol{v}_{\text{pu}}^{\text{dq0}} V_{\text{b}} + W_{\text{pu}}\omega_{\text{b}}\boldsymbol{i}_{\text{pu}}^{\text{dq0}} I_{\text{b}} - \frac{r_{\text{pu}}Z_{\text{b}}}{l_{\text{pu}}L_{\text{b}}}\boldsymbol{i}_{\text{pu}}^{\text{dq0}} I_{\text{b}}. \tag{50}$$

Rearranging using $\frac{Z_{\text{b}}}{L_{\text{b}}} = \omega_{\text{b}}$ gives,

$$\frac{d}{dt}\left(\boldsymbol{i}_{\text{pu}}^{\text{dq0}}\right) = \frac{\omega_{\text{b}}}{l_{\text{pu}}}\boldsymbol{v}_{\text{pu}}^{\text{dq0}} + W_{\text{pu}}\omega_{\text{b}}\boldsymbol{i}_{\text{pu}}^{\text{dq0}} - \frac{r_{\text{pu}}\omega_{\text{b}}}{l_{\text{pu}}}\boldsymbol{i}_{\text{pu}}^{\text{dq0}}, \tag{51}$$

which can be expanded as,

$$\dot{i}^{\text{d}} = \frac{\omega_{\text{b}}}{l_{\text{pu}}}v^{\text{d}} + \omega_{\text{pu}}\omega_{\text{b}}i^{\text{q}} - \frac{r_{\text{pu}}\omega_{\text{b}}}{l_{\text{pu}}}i^{\text{d}} \tag{52}$$

$$\dot{i}^{\text{q}} = \frac{\omega_{\text{b}}}{l_{\text{pu}}}v^{\text{q}} - \omega_{\text{pu}}\omega_{\text{b}}i^{\text{d}} - \frac{r_{\text{pu}}\omega_{\text{b}}}{l_{\text{pu}}}i^{\text{q}}. \tag{53}$$

Now consider a balanced three-phase Y-connected shunt capacitor bank. Capacitor currents $\boldsymbol{i}^{\text{abc}}$ and line-to-neutral voltages $\boldsymbol{v}^{\text{abc}}$ are related through,

$$\boldsymbol{i}^{\text{abc}} = C\frac{d}{dt}\left(\boldsymbol{v}^{\text{abc}}\right). \tag{54}$$

Analysis similar to above yields,

$$\frac{d}{dt}\left(\boldsymbol{v}_{\text{pu}}^{\text{dq0}}\right) = \frac{\omega_{\text{b}}}{c_{\text{pu}}}\boldsymbol{i}_{\text{pu}}^{\text{dq0}} + W_{\text{pu}}\omega_{\text{b}}\boldsymbol{v}_{\text{pu}}^{\text{dq0}}, \tag{55}$$

which can be written,

$$\dot{v}^{\text{d}} = \frac{\omega_{\text{b}}}{c_{\text{pu}}}i^{\text{d}} + \omega_{\text{pu}}\omega_{\text{b}}v^{\text{q}} \tag{56}$$

$$\dot{v}^{\text{q}} = \frac{\omega_{\text{b}}}{c_{\text{pu}}}i^{\text{q}} - \omega_{\text{pu}}\omega_{\text{b}}v^{\text{d}}. \tag{57}$$

APPENDIX B

From (35), series impedances and shunt admittances of the network are dependent on the steady-state frequency ω_{ss}. Therefore the network admittance matrix can be written $Y(\omega_{\text{ss}}) = G(\omega_{\text{ss}}) + jB(\omega_{\text{ss}})$. With ω_{ss} as an extra variable, the power flow equations take the form,

$$\begin{aligned}\mathcal{P}_i(\theta, V, \omega_{\text{ss}}) = V_i \sum_{k=1}^{n} V_k \Big(& G_{ik}(\omega_{\text{ss}})\cos\theta_{ik} \\ & + B_{ik}(\omega_{\text{ss}})\sin\theta_{ik}\Big) - P_i^{sp}(\omega_{\text{ss}}) = 0\end{aligned} \tag{58}$$

$$\begin{aligned}\mathcal{Q}_i(\theta, V, \omega_{\text{ss}}) = V_i \sum_{k=1}^{n} V_k \Big(& G_{ik}(\omega_{\text{ss}})\sin\theta_{ik} \\ & - B_{ik}(\omega_{\text{ss}})\cos\theta_{ik}\Big) - Q_i^{sp}(\omega_{\text{ss}}) = 0,\end{aligned} \tag{59}$$

where $P_i^{sp}(\omega_{\text{ss}})$ and $Q_i^{sp}(\omega_{\text{ss}})$ take into account the frequency dependence of the sources and loads. Such source/load dependence is common [36], [37] whereas the frequency dependence of admittances $G(\omega_{\text{ss}}) + jB(\omega_{\text{ss}})$ is novel.

Solving this modified power flow requires the partial derivatives,

$$\frac{\partial \mathcal{P}_i}{\partial \omega_{\text{ss}}} = \sum_{k=1}^{n}\left(\frac{\partial \mathcal{P}_i}{\partial G_{ik}}\frac{\partial G_{ik}}{\partial \omega_{\text{ss}}} + \frac{\partial \mathcal{P}_i}{\partial B_{ik}}\frac{\partial B_{ik}}{\partial \omega_{\text{ss}}}\right) - \frac{dP_i^{sp}(\omega_{\text{ss}})}{d\omega_{\text{ss}}} \tag{60}$$

$$\frac{\partial \mathcal{Q}_i}{\partial \omega_{\text{ss}}} = \sum_{k=1}^{n}\left(\frac{\partial \mathcal{Q}_i}{\partial G_{ik}}\frac{\partial G_{ik}}{\partial \omega_{\text{ss}}} + \frac{\partial \mathcal{Q}_i}{\partial B_{ik}}\frac{\partial B_{ik}}{\partial \omega_{\text{ss}}}\right) - \frac{dQ_i^{sp}(\omega_{\text{ss}})}{d\omega_{\text{ss}}}, \tag{61}$$

which are straightforward to evaluate.

REFERENCES

[1] *Capabilities and Requirements Definition for Power Electronics Based Technology for Secure and Efficient System Operation and Control*, Cigre Tech. Brochure 821, document JWG C2/B4.38, 2020.

[2] R. Teodorescu, M. Liserre, and P. Rodriguez, *Grid Converters For Photovoltaic and Wind Power Systems*. Hoboken, NJ, USA: Wiley, 2011.

[3] F. Milano, F. Dörfler, G. Hug, D. J. Hill, and G. Verbič, "Foundations and challenges of low-inertia systems (invited paper)," in *Proc. Power Syst. Comput. Conf. (PSCC)*, Jun. 2018, pp. 1–25.

[4] B. Kroposki et al., "Achieving a 100% renewable grid: Operating electric power systems with extremely high levels of variable renewable energy," *IEEE Power Energy Mag.*, vol. 15, no. 2, pp. 61–73, Mar./Apr. 2017.

[5] Y. Li, Y. Gu, and T. Green, "Revisiting grid-forming and grid-following inverters: A duality theory," *IEEE Trans. Power Syst.*, vol. 37, no. 6, pp. 4541–4554, Nov. 2022.

[6] *Addressing the System Strength Gap in SA*, Econ. Eval. Rep., ElectraNet, Adelaide, SA, Australia, Feb. 2019.

[7] *Electranet Contingent Project: Main Grid System Strength*, Australian Energy Regulator, Melbourne, VIC, Australia, Aug. 2019.

[8] J. Matevosyan et al., "Grid-forming inverters," *IEEE Power Energy Mag.*, pp. 89–98, November/Dec. 2019.

[9] Y. Lin et al., "Research roadmap on grid-forming inverters," Nat. Renew. Energy Lab., Golden, CO, USA, Tech. Rep. NREL/TP-5D00-73476, Nov. 2020.

[10] J. Matevosyan et al., "Grid-forming technology in energy systems integration," Task Force High Share Inverter-Based Gener., Energy Syst. Integr. Group, Reston, VA, USA, Tech. Rep., Mar. 2022.

[11] F. Blaabjerg, R. Teodorescu, M. Liserre, and A. V. Timbus, "Overview of control and grid synchronization for distributed power generation systems," *IEEE Trans. Ind. Electron.*, vol. 53, no. 5, pp. 1398–1409, Oct. 2006.

[12] X. Wang, M. Taul, H. Wu, Y. Liao, F. Blaabjerg, and L. Harnefors, "Grid-synchronization stability of converter-based resources—An overview," *IEEE Open J. Ind. Appl.*, vol. 1, pp. 115–134, 2020.

[13] S. D'Arco, J. A. Suul, and O. B. Fosso, "A virtual synchronous machine implementation for distributed control of power converters in smart grids," *Electr. Power Syst. Res.*, vol. 122, pp. 180–197, May 2015.

[14] I. A. Hiskens and E. M. Fleming, "Control of inverter-connected sources in autonomous microgrids," in *Proc. Amer. Control Conf.*, Jun. 2008, pp. 586–590.

[15] M. Surprenant, I. Hiskens, and G. Venkataramanan, "Phase locked loop control of inverters in a microgrid," in *Proc. IEEE Energy Convers. Congr. Expo.*, Sep. 2011, pp. 667–672.

[16] D. Venkatramanan, M. Singh, O. Ajala, A. Domínguez-García, and S. Dhople, "Integrated system models for networks with generators & inverters," in *Proc. Symp. Bulk Power Syst. Dyn. Control (IREP)*, Banff, AB, Canada, Jul. 2022, pp. 1–17.

[17] *IEEE Standard Electrical Power System Device Function Numbers, Acronyms, and Contact Designations*, IEEE Standard C37.2-2008, 2008.

[18] W. Du, R. H. Lasseter, and A. S. Khalsa, "Survivability of autonomous microgrid during overload events," *IEEE Trans. Smart Grid*, vol. 10, no. 4, pp. 3515–3524, Jul. 2019.

[19] W. Du et al., "A comparative study of two widely used grid-forming droop controls on microgrid small-signal stability," *IEEE J. Emerg. Sel. Topics Power Electron.*, vol. 8, no. 2, pp. 963–975, Jun. 2020.

[20] *IEEE Standard for Interconnection and Interoperability of Distributed Energy Resources With Associated Electric Power Systems Interfaces*, IEEE Standard 1547-2018, IEEE Standards Coordinating Committee 21, Feb. 2018.

[21] A. Marinopoulos, F. Papandrea, M. Reza, S. Norrga, F. Spertino, and R. Napoli, "Grid integration aspects of large solar PV installations: LVRT capability and reactive power/voltage support requirements," in *Proc. IEEE Trondheim PowerTech*, Trondheim, Norway, Jun. 2011, pp. 1–8.

[22] J. Blackburn, *Protective Relaying Principles and Applications*, 2nd ed. New York, NY, USA: Marcel Dekker, 1998.

[23] G. Goodwin, S. Graebe, and M. Salgado, *Control System Design*. Upper Saddle River, NJ, USA: Prentice-Hall, 2001.

[24] N. Pogaku, M. Prodanovic, and T. C. Green, "Modeling, analysis and testing of autonomous operation of an inverter-based microgrid," *IEEE Trans. Power Electron.*, vol. 22, no. 2, pp. 613–625, Mar. 2007.

[25] M. Prodanovic and T. C. Green, "Control and filter design of three-phase inverters for high power quality grid connection," *IEEE Trans. Power Electron.*, vol. 18, no. 1, pp. 373–380, Jan. 2003.

[26] J. Schiffer, D. Zonetti, R. Ortega, A. Stanković, T. Sezi, and J. Raisch, "A survey on modeling of microgrids—From fundamental physics to phasors and voltage sources," *Automatica*, vol. 74, pp. 135–150, Dec. 2016.

[27] I. A. Hiskens and P. J. Sokolowski, "Systematic modeling and symbolically assisted simulation of power systems," *IEEE Trans. Power Syst.*, vol. 16, no. 2, pp. 229–234, May 2001.

[28] G. Strang, *Linear Algebra and Its Applications*, 3rd ed. Orlando, FL, USA: Harcourt Brace Jovanovich, 1988.

[29] M. Gibbard, P. Pourbeik, and D. Vowles, *Small-Signal Stability, Control and Dynamic Performance of Power Systems*. Adelaide, SA, Australia: Univ. Adelaide Press, 2015.

[30] I. A. Hiskens and M. A. Pai, "Trajectory sensitivity analysis of hybrid systems," *IEEE Trans. Circuits Syst. I, Fundam. Theory Appl.*, vol. 47, no. 2, pp. 204–220, Feb. 2000.
[31] P. Kokotovic and H. K. Khalil, Eds., *Singular Perturbation in Systems and Control*. New York, NY, USA: IEEE Press, 1986.
[32] S. Jafarpour, V. Purba, B. B. Johnson, S. V. Dhople, and F. Bullo, "Singular perturbation and small-signal stability for inverter networks," *IEEE Trans. Control Netw. Syst.*, vol. 9, no. 2, pp. 979–992, Jun. 2022.
[33] F. L. Pagola, I. J. Perez-Arriaga, and G. C. Verghese, "On sensitivities, residues and participations: Applications to oscillatory stability analysis and control," *IEEE Trans. Power Syst.*, vol. 4, no. 1, pp. 278–285, Feb. 1989.
[34] P. Anderson, *Series Compensation of Power Systems*. Encinitas, CA, USA: PBLSH!, 1996.
[35] C. Canizares et al., "Benchmark systems for small-signal stability analysis and control," IEEE Power Energy Soc., Piscataway, NJ, USA, Tech. Rep. PES-TR18, Aug. 2015.
[36] D. J. Hill, "On the equilibria of power systems with nonlinear loads," *IEEE Trans. Circuits Syst.*, vol. 36, no. 11, pp. 1458–1463, Nov. 1989.
[37] S. V. Dhople, Y. C. Chen, A. Al-Digs, and A. D. Dominguez-Garcia, "Reexamining the distributed slack bus," *IEEE Trans. Power Syst.*, vol. 35, no. 6, pp. 4870–4879, Nov. 2020.

SIJIA GENG (Member, IEEE) received her Ph.D. degree in electrical and computer engineering from the University of Michigan, Ann Arbor, MI, USA, in 2022, and was the recipient of a Barbour Scholarship. She received the M.S. degrees in mathematics and in electrical and computer engineering, both in 2021, also from the University of Michigan. She is currently an Assistant Professor with the Department of Electrical and Computer Engineering at Johns Hopkins University, Baltimore, MD, USA. Prior to joining Johns Hopkins University, she was a Postdoctoral Associate at the Massachusetts Institute of Technology, Cambridge, MA, USA. Her research interests include analysis, control, and optimization of power and energy systems, with a focus on grid-integration of renewable and distributed energy resources.

IAN A. HISKENS (Fellow, IEEE) is currently the Vennema Professor of engineering with the Department of Electrical Engineering and Computer Science, University of Michigan, Ann Arbor. He has held prior appointments with the Queensland electricity supply industry, and various universities in Australia and USA. His research interests lie at the intersection of power system analysis and systems theory, with recent activity focused largely on integration of renewable generation and controllable loads. He is involved in numerous IEEE activities in the Power and Energy Society, the Control Systems Society, the Circuits and Systems Society, and the Smart Grid Initiative, and has served as the VP-Finance for the IEEE Systems Council. He is a fellow of Engineers Australia. He is a Chartered Professional Engineer in Australia, and the 2020 recipient of the M.A. Sargent Medal from Engineers Australia. He is a member of the Editorial Board of the PROCEEDINGS OF THE IEEE.